Slope-Constrained Orography (SCO v1.0) for explicit discrete-slope control in terrain preprocessing: a case study with WRF-ARW (v4.6.1)

Yulong Ma[1], Xingwen Jiang[2,3], Lin Mu[1], and Zhiwei Heng[2,3]

[1]College of Life Sciences and Oceanography, Shenzhen University, Shenzhen, 518055, China
[2]Heavy Rain and Drought-Flood Disasters in Plateau and Basin Key Laboratory of Sichuan Province, ~~Institute of Tibetan Plateau Meteorology, China Meteorological Administration,~~ Chengdu, 610072, China
[3]Institute of Tibetan Plateau Meteorology, ~~Chinese Academy of~~ China Meteorological ~~Sciences~~ Administration, ~~Beijing~~ Chengdu, ~~100081~~ 610072, China

Correspondence: Xingwen Jiang (jiangxingwen@cma.gov.cn) and Lin Mu (mulin@szu.edu.cn)

Abstract. Kilometre-scale Weather Research and Forecasting (WRF) simulations over terrain with steep slopes often require strong smoothing to prevent numerical instability, but conventional domain-wide filters alter terrain at every grid point, regardless of whether local slopes require reduction. Slope-Constrained Orography (SCO) is an offline terrain preprocessing method that prescribes a target slope angle θ and adjusts only those grid points whose eight-neighbour elevation differences exceed the implied bound, leaving the remaining terrain unchanged ~~while permitting stable numerical integration~~. By prescribing the slope constraint directly, SCO ~~replaces the trial-and-error of filter-based smoothing with a single, geometrically interpretable control parameter~~ provides a geometrically interpretable primary user-facing parameter for terrain construction and stability testing. In a 1 km WRF case over the highly complex terrain of the southeastern Tibetan Plateau, the least-modified stable SCO member among those tested modifies 14 % of points with a mean elevation change of 8.2 m, compared with 100 % modification and 108.1 m for the corresponding WRF Preprocessing System (WPS) member. The ~~stable SCO member~~ successful SCO configuration produces lower near-surface wind and temperature errors in this case~~, consistent with improved terrain representation.~~ .

1 Introduction

Complex terrain exerts strong control on boundary-layer flow, thermally driven circulations, and orographic precipitation (Raderschall et al., 2008; Cannon et al., 2017; Díaz-Fernández et al., 2025), motivating the use of kilometre-scale grids to resolve ridge–valley structure. In terrain-following coordinate models such as the Weather Research and Forecasting model (WRF; Skamarock et al., 2019), the large elevation differences that arise on kilometre-scale grids over complex terrain amplify horizontal pressure-gradient errors and can trigger numerical instability within a few time steps (Mahrer, 1984; Klemp et al., 2003; Zängl et al., 2004). Terrain preprocessing is therefore necessary, but the smoothing required to prevent instability routinely modifies terrain well beyond the grid points that actually govern stability.

In the standard WRF Preprocessing System (WPS) workflow, `geogrid` applies a single pass of `smth-desmth_special` smoothing to the terrain field across the entire domain. Over steep terrain at kilometre-scale grid spacing, one pass is often insufficient, and users must increase the pass count, an integer parameter with no direct geometric correspondence to the resulting slope field. The maximum discrete slope that emerges depends on the raw terrain, the grid spacing, and the number of passes, and can only be diagnosed after the smoothing is complete. Because the filter updates every grid point at each iteration, terrain changes propagate far from the locations that control stability. Successive iterations yield diminishing reductions in peak slope, and stability can only be verified by completing a trial integration.

Modifying the vertical coordinate offers an alternative path to accommodating steep slopes (Park et al., 2019; Ma and Liu, 2017), but localised terrain adjustments have also been explored within conventional preprocessing. Sheridan et al. (2023) blended lightly and heavily smoothed terrain across steep-slope regions; Raluy-López et al. (~~2025~~ 2026) applied a local Gaussian filter only to grid points exceeding a slope threshold; and Le Bouëdec et al. (2025) posed terrain adjustment as a constrained optimisation problem with prescribed slope bounds. Slope-Constrained Orography (SCO) follows a similar motivation: it prescribes a target slope angle θ as the ~~sole control variable~~ primary user-facing parameter and adjusts only those grid points whose eight-neighbour elevation differences exceed the implied bound, leaving the rest of the terrain unchanged ~~while maintaining stable numerical integration~~.

This study introduces SCO v1.0 and evaluates it against standard WPS smoothing in 1 km Advanced Research WRF (WRF-ARW) v4.6.1 simulations over the highly complex terrain of the southeastern Tibetan Plateau. Three questions guide the evaluation: (1) can a prescribed-slope approach produce stable 48 h integrations with substantially less terrain modification than domain-wide smoothing, (2) how do the two methods differ in slope-field structure near the stability boundary, and (3) ~~do those differences affect~~ how do near-surface forecast ~~error~~ errors compare between their successful configurations in this case?

Figure 1 has been moved to Sect. 2.2; changes to its caption are marked there.

2 Method and WRF implementation

2.1 Overview

The example description has been moved to the end of Sect. 2.2; wording changes are marked there.

SCO adjusts terrain elevation on a structured grid ~~so that no~~ using working bounds on eight-neighbour elevation ~~difference exceeds the bound implied by~~ differences derived from a prescribed slope angle θ. ~~For a given grid spacing, the bound follows directly from θ, so candidate terrain fields can be generated offline after `geogrid` and before `metgrid` without modifying the WRF dynamical core.~~ Water bodies and lateral boundaries remain fixed throughout. The adjustment proceeds through weighted pairwise projection. Whenever the elevation difference across a neighbour pair exceeds ~~the~~ a local bound, the solver redistributes the excess between the two endpoints in proportion to their mobility weights~~, keeping water bodies and lateral boundaries fixed. It cycles through all neighbour pairs across eight directions and iterates until every constraint is satisfied within tolerance. An octagonal correction ensures directional isotropy across the eight-neighbour stencil (Appendix A1~~. The bounds include a conservative geometric scaling, explained in Sect. 2.2. Inner stopping conditions and a separate outer ac-

ceptance test determine when iteration ends (Sect. 2.3). The implementation assumes uniform grid spacing ($\Delta x = \Delta y$) ~~and constrains elevation differences rather than curvature; curvature constraints are left as a possible extension (Sect. 5).~~.

Because SCO operates on the standard `geo_em` files produced by `geogrid`, it integrates easily into the existing WPS pipeline between `geogrid` and `metgrid` with no modifications to the WRF source code. Here, `geogrid` interpolates static geographical data, including terrain, to the model grids, while `metgrid` interpolates meteorological fields horizontally to the same grids. The Python implementation reads and writes `geo_em.d0X.nc` directly and is used here for both offline diagnostics and terrain construction. Source code, documentation, and a worked example are archived on Zenodo (see Code and data availability).

2.2 Discrete slope metric and constraint derivation

~~Three slope quantities govern the constraint and its verification.~~ The target angle θ is the user-prescribed ~~control variable. The effective ceiling θ_{eff} is the slightly lower angle that results from enforcing an isotropic octagonal bound on the discrete eight-neighbour stencil (Appendix A1). The diagnosed maximum $S_{\max,\text{int}}$ is the largest discrete slope found over the active interior after the solver converges. Their ordering is $S_{\max,\text{int}} \lesssim \theta_{\text{eff}} < \theta$.~~

slope parameter. Let $h_{i,j}$ denote terrain height on a grid with spacing Δx. The local eight-neighbour discrete slope angle is

$$S_{i,j} = \max_{(m,n)\in\mathcal{N}_8(i,j)} \arctan\left(\frac{|h_{m,n} - h_{i,j}|}{d_{(i,j),(m,n)}}\right), \tag{1}$$

where $d = \Delta x$ for cardinal neighbours and $d = \sqrt{2}\,\Delta x$ for diagonal neighbours. The eight neighbours comprise the four cardinal points $(i \pm 1, j)$, $(i, j \pm 1)$ and the four diagonal points $(i \pm 1, j \pm 1)$. Taking the maximum detects an exceedance in any sampled direction; averaging could conceal a single steep pair. The maximum over ~~active interior points (Sect. 2.3)~~ the active interior is denoted $S_{\max,\text{int}}$. This interior consists of land points with mobility weight $w > 0.5$, excluding the frozen rim and the outer part of the boundary taper.

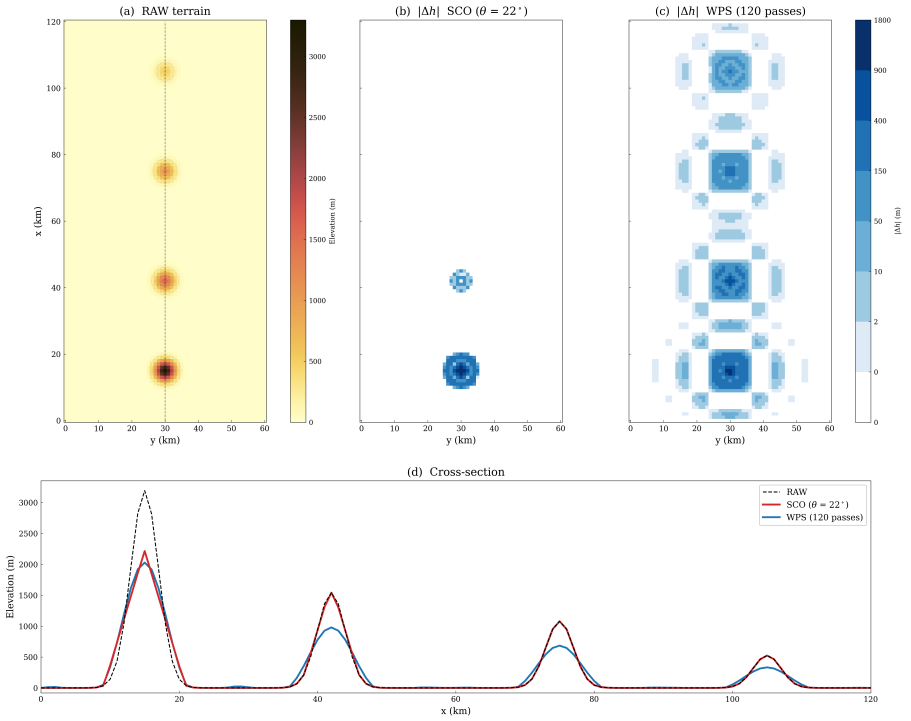
~~The constraint bound follows from requiring isotropy across the stencil. If the cardinal elevation-difference bound is set directly to~~ Cardinal and diagonal bounds of $\Delta x \tan\theta$ ~~, the diagonal directions remain slightly under-constrained. The octagonal correction (Appendix A1) removes that anisotropy:~~ and $\sqrt{2}\,\Delta x \tan\theta$ each correspond to θ in their sampled direction. SCO multiplies both by $\cos(\pi/8)$, giving the initial cardinal bound

$$\Delta h^{(0)}_{\max} = \Delta x \, \tan\theta \, \cos(\pi/8). \tag{2}$$

The diagonal bound is ~~then~~ $\sqrt{2}\,\Delta h^{(0)}_{\max}$. ~~Because the corrected cardinal bound is tighter than the uncorrected value, a converged solution satisfies $S_{i,j} < \theta$ everywhere in the active interior. The effective discrete ceiling~~ This common factor is a conservative geometric scaling for a locally planar surface: the gradient direction is within $\pi/8$ of a sampled direction, so satisfaction of all scaled bounds implies $|\nabla h| \le \tan\theta$ for that plane (Appendix A1). The scaling does not remove the directional anisotropy of the eight-neighbour stencil.

The angle corresponding to the initial working bounds is

$$\theta_{\text{eff}} = \arctan\big[\cos(\pi/8)\,\tan\theta\big], \tag{3}$$



Moved from the end of Sect. 1.

Figure 1. Idealised terrain fields used to contrast SCO and WPS smoothing. Four Gaussian cones ($\sigma = 2.0\,\mathrm{km}$) with peak slopes of 43°, 24°, 18°, and 9° are placed on a flat plain at $\Delta x = 1\,\mathrm{km}$. The ~~effective discrete ceiling~~ angle of the initial working bounds corresponding to $\theta = 22°$ is $\theta_{\mathrm{eff}} = 20.5°$. (a) RAW terrain; the dashed line marks the cross-section in (d). (b) Absolute elevation change $|\Delta h|$ after SCO with $\theta = 22°$. (c) Absolute elevation change $|\Delta h|$ after 120 passes of WPS `smth-desmth_special`. (d) Cross-section through the cone centres.

and the linear approximation $\theta_{\mathrm{eff}} \approx 0.93\theta$ holds to within $0.1°$ over 18°–26°. ~~The approximately 7 % gap between~~ Local tightening can reduce the working bounds further. A field that fully satisfies the initial bounds has $S_{\max,\mathrm{int}} \leq \theta_{\mathrm{eff}}$, apart from numerical tolerance, but acceptance at the nominal angle θ ~~and θ_{eff} is intrinsic to the octagonal geometry: after convergence, $S_{\max,\mathrm{int}}$ settles near θ_{eff} rather than near θ (Table 1).~~ does not establish convergence to those bounds. The idealised example in Fig. 1 illustrates the basic contrast: SCO modifies only the cones whose slopes violate the ~~bound~~ working bounds, whereas WPS smoothing alters all four. RAW denotes the unsmoothed reference terrain.

2.3 Iterative projection solver

Each grid point carries a mobility weight $w_{i,j} \in [0, 1]$ that controls how freely the solver may adjust its elevation. Water points receive $w = 0$ and are never modified. The outermost r rows and columns are likewise frozen at $w = 0$; across the next t rows

and columns inward, a cosine taper raises w smoothly from 0 to 1. All remaining interior land points carry $w = 1$. The ~~values~~ fixed settings used here are $r = 3$ and $t = 5$.

Grid points with $w > 0.5$ define the *active interior*. This threshold coincides with the midpoint of the cosine taper and marks the region over which $S_{\max,\mathrm{int}}$ is evaluated and ~~convergence is checked~~ the outer acceptance test is applied. Boundary points ($w \le 0.5$) may retain residual slope violations~~; these are diagnosed separately~~, but do not enter the ~~convergence criterion.~~ outer acceptance test or local tightening. The inner monitor includes all neighbour pairs with $w_p + w_q > 10^{-6}$, including pairs adjoining frozen points.

The solver sweeps four classes of neighbour pairs in sequence (horizontal, vertical, main diagonal, anti-diagonal) using a red–black decomposition for vectorised execution. For a neighbour pair (p, q) ~~whose elevation difference~~, the working bound is $L_{pq} = (d_{pq}/\Delta x)\min(f_p, f_q)\Delta h^{(0)}_{\max}$, where $d_{pq} = \Delta x$ for cardinal pairs and $\sqrt{2}\,\Delta x$ for diagonal pairs. The local tightening factor f is initially 1. It changes the bound, whereas the mobility weight w determines how the correction is shared. When the height difference $\delta = h_q - h_p$ ~~exceeds the local bound~~ exceeds L_{pq} in magnitude and the pair is movable, the excess

$$e = \delta - \mathrm{sgn}(\delta)\, L_{pq} \tag{4}$$

is redistributed according to the endpoint mobilities:

$$h_p \leftarrow h_p + e\,\frac{w_p}{w_p + w_q}, \qquad h_q \leftarrow h_q - e\,\frac{w_q}{w_p + w_q}. \tag{5}$$

When both endpoints share the same mobility the pair mean is conserved. When they differ, as in the transition zone, the more mobile endpoint absorbs the larger share and the pair mean shifts toward the less mobile point. Frozen points ($w = 0$) never move. ~~Because each red–black subset contains only non-overlapping pairs, the maximum violation within each pair class cannot increase during a sweep.~~

~~Where steep slopes cluster, a single pass through all four pair classes can leave small residual violations.~~ An outer loop ~~addresses this by progressively tightening~~ progressively tightens the local bound at each active interior point through ~~a~~ the factor $f_{i,j}$~~, initialised to 1~~:

$$\Delta h_{\max,i,j} = f_{i,j}\,\Delta h^{(0)}_{\max}. \tag{6}$$

For sweep s, the monitored quantity E_s is the largest positive pairwise exceedance $\max(|h_q - h_p| - L_{pq}, 0)$ encountered over movable pairs during the sweep. The inner stopping conditions are $E_s < 0.1$ m, stagnation, or the limit of 500 sweeps. Stagnation means $E_s \ge 0.999 E_{s-1}$ for three consecutive comparisons. Persistent exceedances beside the frozen boundary can trigger this exit before the active interior has fully converged.

After each inner solve, ~~any active interior point that still exceeds θ has its factor reduced in proportion to the overshoot:~~ the outer acceptance test checks $S_{\max,\mathrm{int}} \le \theta + 0.01°$. If it is not met, the factors at active interior points with $S_{i,j} > \theta$ are tightened as

$$f_{i,j} \leftarrow \max\!\left(f_{i,j}\,\beta\,\frac{\theta}{S_{i,j}},\; f_{\min}\right), \tag{7}$$

where $\beta = 0.97$ damps oscillations and $f_{\min} = 0.30$ prevents over-tightening.

The outer loop terminates when $S_{\max,\mathrm{int}} \le \theta + 0.01°$ are fixed. The next inner solve uses the updated bounds. The outer loop ends on acceptance or after 10 iterations. Because the stopping rule references θ rather than θ_{eff}, the residual gap between $S_{\max,\mathrm{int}}$ and θ_{eff} reflects the criterion itself rather than incomplete convergence. Each inner solve runs for at most 500 sweeps with a convergence tolerance of 0.1 m on the maximum pairwise exceedance. rounds. The full pseudocode and parameter values are given in Appendix A2. All offline diagnostics and figures in this study use `max_outer` = 10, `max_sweeps` = 500, `inner_tol` = 0.1 m, and `outer_tol_deg` = 0.01°. These are also the module defaults in the released code, which users may adjust for other domains.

2.4 Offline diagnostics

Constraint compliance is measured by $S_{\max,\mathrm{int}}$, the maximum of $S_{i,j}$ over the active interior. The near-critical count records spatial clustering near the slope ceiling: it The offline diagnostics quantify achieved slopes, the magnitude and extent of terrain modification, and retained small-scale terrain structure. The near-maximum count is the number of active interior points whose $S_{i,j}$ falls within $\varepsilon = 0.2°$ of below the member's own $S_{\max,\mathrm{int}}$. The tolerance $\varepsilon = 0.2°$ exceeds the residual convergence gap (approximately 0.01°) while remaining small enough to isolate near-ceiling clustering. A large count indicates that many grid points lie near the ceiling. It describes concentration in the slope distribution, not geographic clustering.

Terrain fidelity is characterised by the mean absolute elevation change, $\mathrm{MAE}_h = \langle |h_{\mathrm{new}} - h_{\mathrm{raw}}| \rangle$, over interior land points, which gives the domain-mean elevation displacement, and by the . The modified-area fraction , is the proportion of those points where $|h_{\mathrm{new}} - h_{\mathrm{raw}}| > 0.1\,\mathrm{m}$. MAE_h measures the typical magnitude of elevation change; the . The modified-area fraction measures how widely those changes spread. Retained short-wave small-scale terrain structure is quantified by the Laplacian RMS: the root-mean-square (RMS) over interior land points of the unnormalised five-point discrete Laplacian second difference

$$L_{i,j} = h_{i+1,j} + h_{i-1,j} + h_{i,j+1} + h_{i,j-1} - 4\,h_{i,j} \tag{8}$$

(in metres). Because the Laplacian On the uniform grid, this difference equals Δx^2 times the discrete Laplacian. Because it responds to second-order terrain structure, it distinguishes terrain fields with similar $S_{\max,\mathrm{int}}$ but different short-wave small-scale content. Ridge-to-valley relief retention along cross-sections is defined as the ratio of the peak-to-valley elevation difference in the processed field to that in RAW.

3 Experimental design

3.1 Study region and model configuration

The test region is the southeastern Tibetan Plateau (Fig. 2), where raw discrete slope angles on a 1 km grid exceed 40° (Table 1). Two one-way-nested WRF-ARW v4.6.1 domains are used. The outer domain (D01) covers the eastern Tibetan Plateau margin and the Sichuan Basin on a 360×360 grid at 3 km spacing; the inner domain (D02) spans the steep plateau–basin transition on a 420×420 grid at 1 km spacing. Both domains use 54 vertical levels with a model top at 50 hPa and the hybrid terrain-following coordinate. ~~The time step is 18 s for D01 and 6 s for D02 for most members, reduced to 12–15 s on D01 for the more heavily smoothed WPS members to maintain numerical stability.~~

D01 supplies the lateral boundary conditions for D02, with no feedback from D02 to D01. D01 terrain is fixed after one WPS `smth-desmth_special` pass; all terrain-treatment differences are confined to D02. Time steps were reduced for the WPS configurations as needed for stability (Fig. 3). With the parent-to-nest time-step ratio fixed at 3, these reductions also change the parent-domain integration.

All simulations are initialised at 0000 UTC (Coordinated Universal Time) 18 July 2025 from ~~ERA5 reanalysis~~ the fifth-generation reanalysis (ERA5) of the European Centre for Medium-Range Weather Forecasts (Hersbach et al., 2020) and integrated for 48 h. Static terrain for the 1 km inner domain is built from the 30 m ~~ASTER~~ Advanced Spaceborne Thermal Emission and Reflection Radiometer (ASTER) Global Digital Elevation Model (GDEM; Tachikawa et al., 2011) by area averaging onto the model grid. The physics configuration is identical across all experiments: Thompson microphysics (Thompson et al., 2008), Rapid Radiative Transfer Model for ~~GCMs~~ general circulation models (RRTMG) radiation (Iacono et al., 2008), the Yonsei University (YSU) planetary boundary layer scheme (Hong et al., 2006), the revised Fifth-Generation Penn State/~~NCAR Mesoscale Model~~ National Center for Atmospheric Research mesoscale model (MM5) Monin–Obukhov surface layer, Noah~~-MP~~ land surface model with multiparameterization options (Noah-MP) (Niu et al., 2011), and gravity-wave drag on D01 only. No cumulus parameterisation is used on either domain. ~~The full~~ A reference WRF namelist is provided in the code repository.

3.2 Terrain members and member selection

~~D01 terrain is fixed after a single WPS `smth-desmth_special` pass; all terrain differences among members are confined to D02.~~ For the WPS pathway, `smth-desmth_special` is applied for N passes to the aggregated D02 terrain, and the member label gives the pass count. Five members are tested: WPS01, WPS60, WPS100, WPS120, and WPS150. SCO members are generated by applying the slope-constrained adjustment (Sect. 2.3) directly to the unsmoothed D02 terrain. Five members span $\theta = 18°$ to 26° at 2° intervals, with the member label giving the target angle. All SCO members share the same solver settings ($r = 3$, $t = 5$, $\beta = 0.97$, $f_{\min} = 0.30$); only θ varies. RAW is retained as an offline reference. A control experiment, W1+SCO24, applies one WPS pass before SCO at $\theta = 24°$ to test whether light pre-smoothing changes the stability outcome at fixed $S_{\max,\mathrm{int}}$.

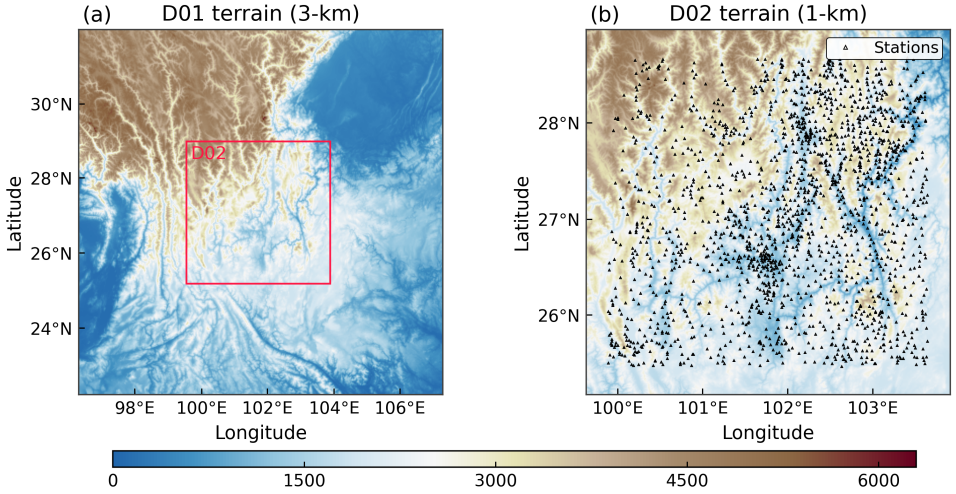


Figure 2. Model domains and observation network. (a) D01 terrain elevation (3 km grid spacing) with the D02 boundary marked. (b) D02 terrain elevation (1 km grid spacing) with the 927 surface stations used for near-surface verification.

The cross-method comparison pairs the least-modified stable member from each method ~~under~~ among the discrete candidates tested under their reported configurations and the same 48 h stability criterion. These selections are neither exact stability limits nor globally optimal terrain solutions. Members are not matched by slope or terrain cost, since neither method offers a natural counterpart at fixed values of these quantities. One additional stable member from each method enters the near-surface evaluation to gauge within-method sensitivity.

3.3 Observations and verification protocol

Near-surface verification uses hourly 10 m wind speed and 2 m temperature from 927 China Meteorological Administration (CMA) surface stations within the D02 interior (Fig. 2b). The denser local network improves spatial sampling in interior valleys, where terrain effects are expected to be strongest.

Stations within 30 grid points of the lateral boundaries are excluded to avoid relaxation-zone contamination, and each retained time series must contain at least 20 % valid observations during the 48 h window. At any given station, the terrain-height difference between members is much smaller than the model-minus-observation elevation offset, so systematic elevation bias largely cancels in the paired comparison. Model fields are bilinearly interpolated to station locations without elevation correction.

The final sample contains 44 200 wind pairs and 44 115 temperature pairs. Inter-member root-mean-square error (RMSE) differences are tested with a two-sided paired t-test across stations, each contributing one time-averaged RMSE value. The test does not account for spatial correlation among nearby stations, so the reported p values should be interpreted as approximate.

Table 1. Terrain members with offline diagnostics and stability outcomes. The control parameter is the WPS pass count N or the SCO target angle θ. For SCO members, θ_{eff} is the ~~effective discrete ceiling under~~ angle corresponding to the ~~octagonal correction~~ initial working bounds (Sect. 2.2). "48 h" ~~indicates whether~~ gives the ~~member completes~~ reported integration outcome under the ~~full~~ stated 48 h ~~integration; all failed members terminate within~~ stability criterion and the ~~first 15 min~~ member-specific configuration (Fig. 3). W1+SCO24 MAE_h is measured relative to its WPS01-smoothed input rather than to RAW, and its modified-area fraction is not directly comparable to the RAW-referenced values of the other members; neither quantity enters the cross-method comparison.

Member	Path	Control	θ_{eff} (°)	$S_{\mathrm{max,int}}$ (°)	MAE_h (m)	Mod. (%)	48 h
RAW	–	–	–	47.73	0	0	–
WPS01	WPS	$N = 1$	–	41.49	30.4	>99.9	fail
WPS60	WPS	$N = 60$	–	26.24	96.4	>99.9	fail
WPS100	WPS	$N = 100$	–	24.44	105[a]	>99.9	fail
WPS120	WPS	$N = 120$	–	24.13	108.1	100.0	pass
WPS150	WPS	$N = 150$	–	23.76	111.9	100.0	pass
SCO18	SCO	$\theta = 18°$	16.7	17.24	17.9	26.0	pass
SCO20	SCO	$\theta = 20°$	18.6	19.31	12.3	19.4	pass
SCO22	SCO	$\theta = 22°$	20.5	21.12	8.2	14.0	pass
SCO24	SCO	$\theta = 24°$	22.4	22.36	5.3	9.9	fail
SCO26	SCO	$\theta = 26°$	24.3	24.26	3.3	6.5	fail
W1+SCO24	Combo	$N = 1$+$\theta = 24°$	22.4	22.36	2.2 [b]	n.a. [b]	fail

[a] WPS100 MAE_h is rounded to the nearest integer. [b] W1+SCO24 MAE_h is measured relative to its WPS01-smoothed input, not relative to RAW; excluded from the cross-method comparison.

4 Results

4.1 Terrain modification and retained structure

Under the common 48 h stability criterion, SCO22 and WPS120 are the least-modified stable members among those tested for the two methods (Table 1). Their terrain costs differ by an order of magnitude. SCO22 modifies 14.0 % of interior land points with $\mathrm{MAE}_h = 8.2$ m; WPS120 ~~, which must alter~~ modifies the entire domain ~~to reach a comparable stability margin,~~ and has $\mathrm{MAE}_h = 108.1$ m (Fig. 3).

SCO22 also retains far more ~~short-wave~~ small-scale terrain structure. Its ~~Laplacian RMS~~ RMS of the five-point second difference reaches 279.8 m, nearly six times the 47.9 m of WPS120. Cross-sections confirm the same pattern: SCO22 retains 97–99 % of the RAW ridge-to-valley relief along two representative transects, compared with 79–86 % for WPS120 (Fig. 4).

All SCO members ~~satisfy the prescribed eight-neighbour bound~~ attain the nominal target θ over the active interior ~~, with achieved $S_{\mathrm{max,int}}$ settling close to θ_{eff} and remaining below θ in every case~~ (Fig. 5). The maxima for SCO24 ~~converges cleanly yet fails within 15 min, whereas SCO22, with a tighter constraint, completes the full 48 h integration. Although the two members also differ in sweep count (24 vs. 10~~ and SCO26 lie close to θ_{eff}, whereas those for SCO18–SCO22 remain above it

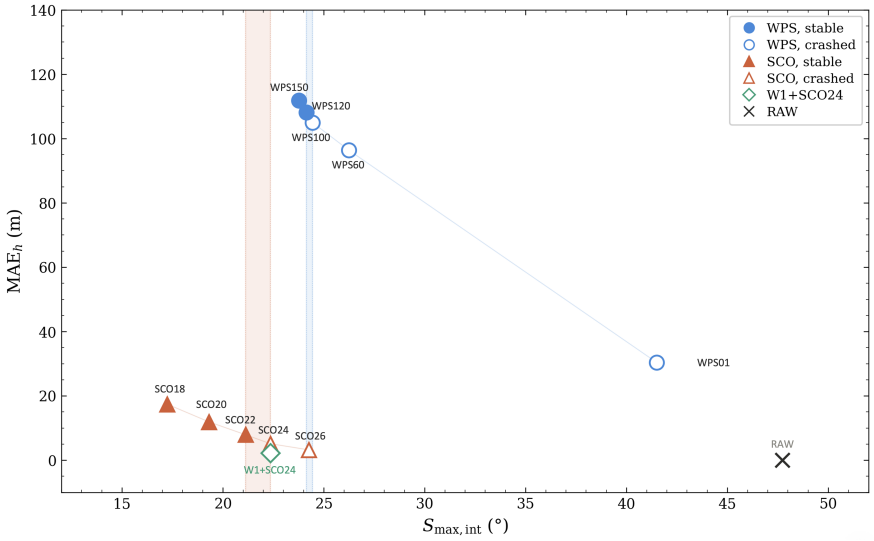


Figure 3. Terrain-member pathways in (MAE_h, $S_{\max,\mathrm{int}}$) space. Filled symbols indicate stable members and open symbols indicate failed members. Shaded bands ~~mark~~ span the ~~stability boundary intervals for each method~~ adjacent passing and failing candidates; the WPS interval also includes a change in time step. For W1+SCO24, MAE_h is referenced to its WPS01 input rather than RAW. Reported D01/D02 time steps: SCO and W1+SCO24, 18/6 s; WPS100, 15/5 s; WPS120 and WPS150, 12/4 s. WPS120 failed at 18/6 s and passed at 12/4 s.

(Table 1; Fig. 5~~b), stability is determined by the resulting terrain field rather than by the convergence behaviour.~~ c). The latter fields pass the outer acceptance test without fully satisfying the tighter internal working bounds, consistent with the stagnation exit described in Sect. 2.3.

4.2 Diagnostics near the stability boundary

~~Every unstable member terminates within the first 15 min with Courant–Friedrichs–Lewy (CFL) violations, indicating that the terrain field, rather than the subsequent meteorological evolution, governs the failure.~~

~~The two methods reach their stability boundaries at different $S_{\max,\mathrm{int}}$ (Table 1; Fig. 3).~~ The WRF integrations with the unstable members terminated prematurely. Along the WPS pathway, WPS100 ($S_{\max,\mathrm{int}} = 24.44°$) fails while WPS120 (24.13°) completes the full 48 h integration ~~, placing the boundary within a 0.31° interval as sampled by the tested members. The SCO boundary is wider:~~ under the reported configurations (Table 1; Fig. 3). Along the SCO pathway, SCO24 (22.36°) fails and SCO22 (21.12°) passes, a sampled passing–failing gap of 1.24°. The ~~two marginal stable members~~ selected stable members, SCO22 and WPS120, differ by 3.0° in peak slope~~, so $S_{\max,\mathrm{int}}$ alone does not account for the different stability outcomes on this domain~~.

At the domain scale, the slope fields ~~surrounding these boundary members~~ of SCO22, SCO24, WPS100 and WPS120 differ sharply. Of the active interior points in SCO24, 15 359 fall within $\varepsilon = 0.2°$ ~~of~~ below its own $S_{\max,\mathrm{int}}$; WPS120 has only 4 (Table 2). The exceedance counts (Fig. 6b) illustrate the same contrast: SCO members drop steeply ~~at the imposed~~

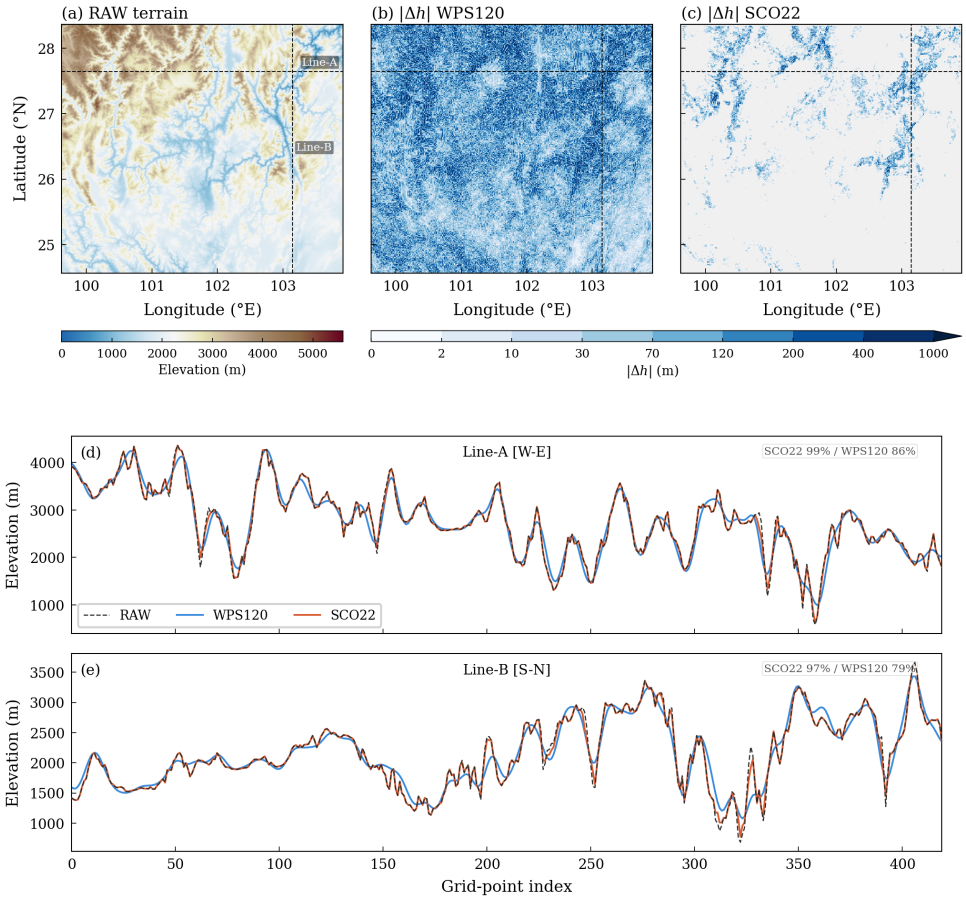


Figure 4. Terrain modification footprint and retained relief. (a) RAW terrain elevation with cross-section locations marked. (b) Absolute elevation change $|\Delta h|$ for WPS120 and (c) for SCO22, shown on the same colour scale (0–1000 m). (d) West–east cross-section A–A′ ($j = 339$) and (e) south–north cross-section B–B′ ($i = 346$). Annotated percentages denote ridge-to-valley relief retained relative to RAW.

~~ceiling~~ near their diagnosed maxima, whereas the WPS tail decays gradually over several degrees. Because repeated smoothing progressively lowers ~~all~~ slopes, few WPS grid points remain near the residual peak.

In the slope probability density functions (PDFs; Fig. 6a), the contrast takes a different form: the WPS distribution falls off gradually in the upper tail, with most grid points well below the peak, while ~~the SCO distribution is truncated sharply at the imposed ceiling and accumulates a dense population just below it. That accumulation follows from the pairwise projection, which stops adjusting each pair as soon as the bound is met~~ SCO24 has a concentrated population near its working bound.

~~All three failing members terminate at the same grid point on a valley-wall feature. Within a~~ Figure 7 compares the local terrain around the reported failure site. Within this 41×41 ~~neighbourhood centred on the failure site (Fig. 7)~~ neighbourhood, SCO24 retains ~~the short-wave~~ small-scale ridge–valley structure and ~~brings many grid points close to the ceiling simultaneously: 604 exceed~~ has 604 grid points above 22°. By contrast, WPS100 presents a narrow band of steep slopes against

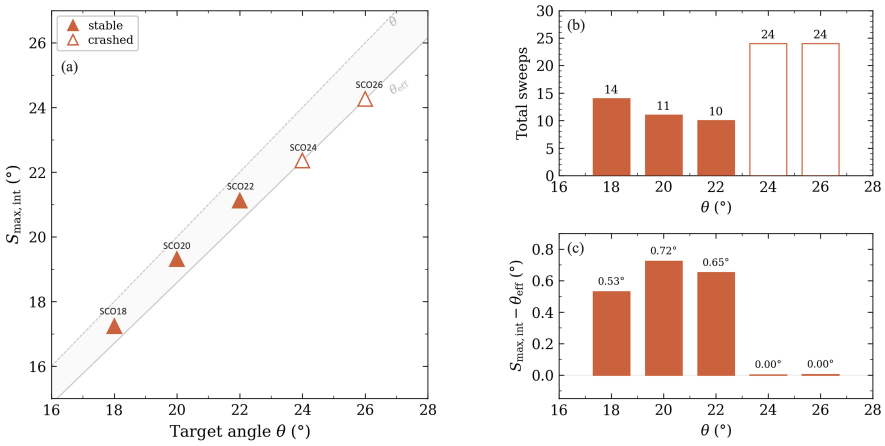


Figure 5. Target θ versus achieved $S_{\mathrm{max,int}}$ for SCO18–SCO26. (a) The ~~dashed~~ solid line marks θ_{eff} and the dashed line θ; filled triangles indicate stable members and open triangles indicate failed members. (b) Total sweep count. (c) ~~Residual~~ Angular difference $S_{\mathrm{max,int}} - \theta_{\mathrm{eff}}$ after the final outer round. The positive differences for SCO18–SCO22 distinguish attainment of the nominal target from convergence to the internal working bounds.

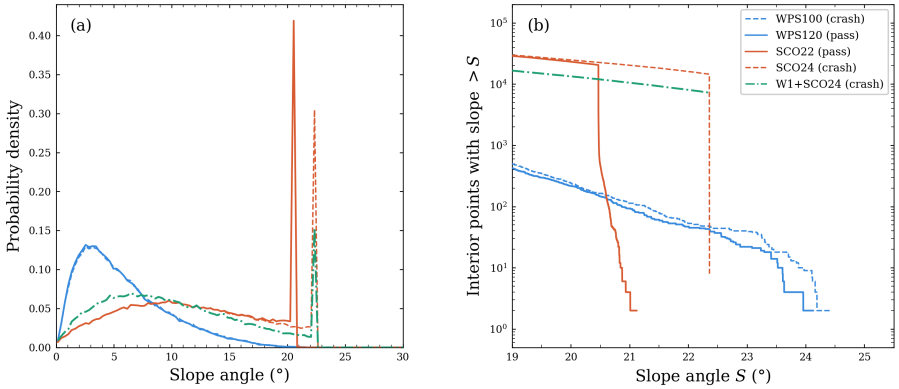


Figure 6. Slope distributions for members near the stability boundary. (a) Probability density functions for WPS100, WPS120, SCO22, SCO24, and W1+SCO24. (b) Exceedance counts: number of active interior grid points with discrete slope exceeding S, shown on a logarithmic vertical axis. The sharp drop-off in the SCO members reflects the ~~imposed slope ceiling~~ slope-constrained adjustment; the gradual tail in the WPS members reflects the progressive nature of domain-wide smoothing.

a smooth background, with only 23 grid points above 22°. ~~The three members share the same failure location, yet the slope fields they present to the dynamical core differ considerably.~~

W1+SCO24 tests whether removing ~~short-wave~~ small-scale terrain structure at fixed $S_{\mathrm{max,int}}$ can produce a stable integration. One WPS pass applied before SCO at $\theta = 24°$ lowers the ~~Laplacian~~ second-difference RMS from 289.6 to 186.7 m and ~~halves the near-critical~~ approximately halves the near-maximum count (from 15 359 to 7 681), while holding $S_{\mathrm{max,int}}$ at 22.36° (Table 2). Row-mean spectra confirm that about 70 % of the power near 2 km wavelength is removed, while the 10 km

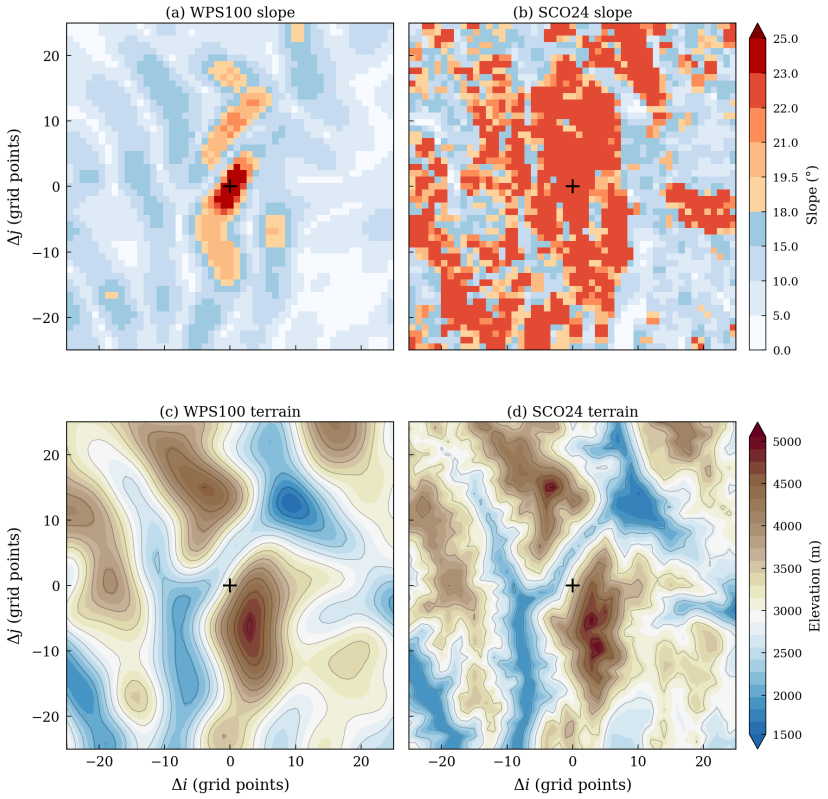


Figure 7. Local slope and elevation fields near the shared crash location (41×41 neighbourhood centred on $i = 50$, $j = 291$, 1-based). (a, b) Discrete slope $S_{i,j}$ for WPS100 and SCO24. (c, d) Terrain elevation for the same members. The cross marks the failure site.

band remains largely intact (Fig. 8). ~~Yet the member still fails within 15 min. Reducing curvature and spectral content without lowering $S_{\max,\mathrm{int}}$ does not produce a stable integration in this case.~~

SCO24 and W1+SCO24 both fail. The tested pre-smoothing was therefore insufficient to restore stability under these settings.

Figure 8 shows SCO22 and SCO24 because they bracket the sampled SCO passing–failing interval; it also compares WPS120 and W1+SCO24. SCO22 and SCO24 retain most of the RAW power near 2 and 10 km, and SCO24 retains more than SCO22; WPS120 removes most of the power in those bands (Table 2). SCO is a nonlinear local adjustment, so its spectral response depends on terrain amplitude and structure, grid spacing and θ rather than on a fixed transfer function. In the tested sequence, lower θ increases terrain modification (Table 1). The slope distributions and second-order diagnostics show that the methods produce different terrain structures beyond the maximum slope. Those properties may influence numerical behaviour, but the present experiments do not isolate their effects.

~~Members with similar or even lower peak slope can thus differ widely in how densely near-ceiling slopes are packed. Whether that packing is causally responsible for the early CFL failure remains a working hypothesis (Sect. 5).~~

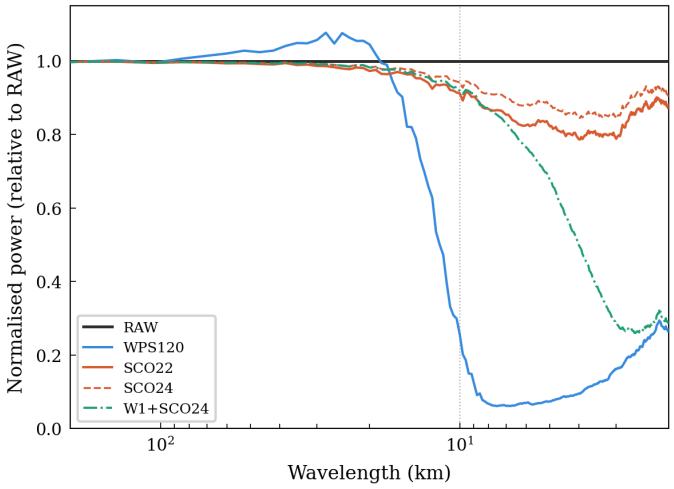


Figure 8. ~~Normalised row-mean power spectral density for RAW, WPS120, SCO22, SCO24, and W1+SCO24.~~ Row-mean terrain power normalised by RAW at each wavenumber for RAW, WPS120, SCO22, SCO24 and W1+SCO24. Wavelength is shown on a logarithmic horizontal axis. Vertical dotted lines mark 2 km and 10 km.

Table 2. Diagnostics for selected members near the ~~stability boundary~~ sampled passing–failing intervals. ~~Near-critical~~ Near-maximum count is the number of active interior points within $\varepsilon = 0.2°$ ~~of~~ below each member's own $S_{\max,\mathrm{int}}$; it describes the slope distribution, not geographic clustering. Second-difference RMS is the RMS of the unnormalised five-point second difference in Eq. (8). Spectral retention is defined relative to RAW at the indicated wavelengths. Outcomes refer to the configurations in Fig. 3.

Member	$S_{\max,\mathrm{int}}$ (°)	~~Near-crit. count~~ Near-maximum count	~~Lapl. RMS (m)~~ Second-difference RMS (m)	2 km ret. (%)	10 km ret. (%)	48 h
WPS100	24.44	2	49.9	27	30	fail
WPS120	24.13	4	47.9	27	25	pass
SCO22	21.12	6	279.8	88	91	pass
SCO24	22.36	15 359	289.6	91	94	fail
W1+SCO24	22.36	7 681	186.7	30	92	fail

4.3 Near-surface verification

~~The four~~ Four stable members (WPS120, WPS150, SCO20, and SCO22) are evaluated against the 927-station network over the full 48 h period (Table 3). Comparing the two least-modified stable members, SCO22 produces lower errors for both variables: wind RMSE is lower by about 0.15 m s^{-1} with a weaker positive bias, and 2 m temperature RMSE is lower by about 0.16 K (Table 3). The error differences between these successful configurations cannot be attributed to D02 terrain alone. The 2 m temperature bias reverses sign between the two members ($\pm$0.17 K) but at this magnitude it is too small to diagnose a systematic difference.

Table 3. Forty-eight-hour near-surface verification. RMSE denotes root-mean-square error. SCO20 and SCO22 show no detectable difference in wind RMSE ($p = 0.97$) or in 2 m temperature RMSE ($p = 0.32$) under ~~a~~ the approximate two-sided paired t-test across stations (Sect. 3.3).

Member	Wind RMSE ($\mathrm{m\,s^{-1}}$)	Wind bias ($\mathrm{m\,s^{-1}}$)	2 m temp. RMSE (K)	2 m temp. bias (K)
WPS120	1.790	+0.854	2.147	−0.168
WPS150	1.779	+0.844	2.194	−0.184
SCO20	1.644	+0.631	1.984	+0.164
SCO22	1.642	+0.620	1.984	+0.165

Within-method differences are much smaller. SCO20 and SCO22 ~~are statistically indistinguishable, and the~~ show no detectable difference in wind and temperature RMSE under the approximate stationwise paired test (Sect. 3.3). The step from WPS120 to WPS150 changes scores only modestly. Because the comparison rests on a single 48 h case, these numbers are specific to the present domain and period.

5 Discussion

SCO meets the stability criterion on this domain with far less terrain alteration than WPS~~, but the two methods also reach their stability boundaries at different $S_{\mathrm{max,int}}$. The spatial arrangement of near-critical slopes contributes to the boundary position alongside the peak value.~~. WPS120 ~~survives at~~ has a higher $S_{\mathrm{max,int}}$ than SCO24, ~~yet~~ and the two members' slope fields differ markedly in how many grid points ~~cluster near the ceiling~~ lie near their respective maxima. The W1+SCO24 control ~~reinforces this interpretation:~~ shows that removing much of the ~~short-wave~~ small-scale structure while holding $S_{\mathrm{max,int}}$ fixed does not recover stability ~~. One possible mechanism is that broad regions of near-ceiling slopes generate spatially coherent pressure-gradient truncation errors, allowing perturbations to grow before the model can dissipate them. Diagnosing the pressure-gradient tendency and vertical velocity fields during the first few time steps would test this hypothesis directly, but falls beyond the terrain-preprocessing focus of the present study.~~ under the tested settings. The diagnostics examined here may not capture all terrain differences relevant to stability. ~~The two methods can produce fields that differ in ways beyond $S_{\mathrm{max,int}}$, near-critical count, and spectral content, and a much denser sampling of the stability boundary or direct diagnosis of pressure-gradient truncation error would be needed to resolve this.~~

The diminishing returns of repeated `smth-desmth_special` passes compound the terrain-cost asymmetry between the two methods (Fig. 3). ~~Short-wave~~ Small-scale terrain is removed much faster than the residual peak slope declines~~, which explains why WPS requires such large terrain changes to reach the stability boundary. Within the stable SCO range~~. Among the evaluated stable SCO members, SCO20 and SCO22 yield nearly identical forecast scores~~, suggesting that once a member is well within the stable regime, further tightening of θ adds little. The practical difference between the two approaches is therefore in the stability-testing workflow itself.~~. A filter-based approach requires the user to choose a pass count, blending factor, or filter width and then inspect the resulting slope field. SCO prescribes θ first ~~, builds the terrain field to satisfy that bound,~~ and uses the same variable to generate candidates, diagnose them offline, test for stability, and select the final member.

On the 420×420 D02 grid used here, each SCO member is generated in under 10 s on a single ~~CPU~~ central processing unit (CPU) core, so the entire five-member θ sweep completes in under a minute.

A practical workflow begins by diagnosing the raw terrain and generating a coarse sequence of θ values. Each field is checked offline for $S_{\max,\mathrm{int}}$, residuals relative to its internal working bounds, and the magnitude and extent of terrain modification. Stability integrations with a fixed model configuration and time step then bracket the sampled passing–failing interval. The interval can be refined if needed, and the least-modified passing member is selected from those tested. The selection must be reassessed when the model configuration changes.

The focus of this study is not on forecast improvement through terrain modification, but on preserving terrain fidelity as far as possible while maintaining numerical stability. ~~All terrain differences among members are confined to D02, so the interaction with the nesting configuration has not been isolated. The current implementation assumes uniform grid spacing, and extending the projection geometry to variable-resolution or unstructured meshes is a separate task.~~ Greater retention of ridge–valley relief and terrain spectral content (Figs. 4 and 8) preserves more of the lower-boundary structure available to force local atmospheric flows. The hourly station evaluation quantifies bulk errors, whereas assessing the realism of resolved flow variability requires complementary diagnostics, as illustrated by Sheridan et al. (2023). Such variability was not evaluated here.

6 Conclusions

SCO prescribes the target slope angle θ as ~~the preprocessing control variable and enforces an~~ its primary user-facing parameter and applies local eight-neighbour ~~elevation-difference bound~~ terrain adjustments between `geogrid` and `metgrid`. ~~Because θ determines the terrain field directly, SCO replaces the trial-and-error of filter-based preprocessing with a single, geometrically interpretable parameter that governs both terrain generation and stability testing~~ The parameter provides a geometrically interpretable way to generate terrain candidates and organise stability tests. On the highly complex terrain of the southeastern Tibetan Plateau at 1 km grid spacing, the least-modified stable SCO member among those tested (SCO22) completes a 48 h integration with $\mathrm{MAE}_h = 8.2$ m and 86 % of interior land points unmodified, compared with $\mathrm{MAE}_h = 108.1$ m and 100 % modification for the least-modified stable WPS member (WPS120).

~~Near the stability boundary, peak slope alone does not determine stability in this case. The diagnostics suggest that the spatial density of near-ceiling slopes also plays a role in setting the boundary position, since members with comparable $S_{\max,\mathrm{int}}$ produce opposite stability outcomes depending on the surrounding slope field. The mechanism remains a working hypothesis, but the contrast in near-ceiling slope density between the two methods is unambiguous~~ SCO22 retains substantially more small-scale terrain structure than WPS120, while the near-boundary candidates show distinct upper-tail slope distributions. The sampled passing range is specific to the tested case and model configuration.

For the successful configurations, SCO22 also produces lower near-surface wind and temperature errors in this 48 h case. Whether this advantage holds across other domains and seasons remains to be tested. ~~Because θ controls both terrain generation and offline testing, SCO condenses the trial-and-error of filter-based preprocessing into a single parameter choice tied directly to the slope metric most relevant to stability, with~~ With each candidate terrain generated in seconds~~.~~, SCO provides an efficient

way to explore the balance between terrain retention and numerical stability. Curvature constraints and packaging SCO as an optional WPS component are possible extensions. The current implementation assumes uniform grid spacing, and extending the projection geometry to variable-resolution or unstructured meshes is a natural next step toward broader applicability.

Appendix A: ~~Octagonal correction~~ Geometric scaling and algorithm summary

A1 ~~Isotropic octagonal correction~~ Conservative scaling for locally planar terrain

~~If the cardinal elevation-difference bound is set directly to $\Delta x \tan\theta$, the eight-neighbour stencil remains rotationally anisotropic. A regular octagon inscribed in a circle of radius $\Delta x \tan\theta$ has apothem $\Delta x \tan\theta \cos(\pi/8)$. Setting the cardinal bound to this apothem gives~~

~~$$\Delta h^{(0)}_{\max} = \Delta x \tan\theta \cos(\pi/8),$$~~

For a locally planar surface with gradient $\boldsymbol{g} = \nabla h$, the neighbour-pair ratio in a unit direction $\boldsymbol{u}$ is $|h_q - h_p|/d_{pq} = |\boldsymbol{g} \cdot \boldsymbol{u}|$. Let $\mathcal{U}_8$ contain the unit vectors along the eight sampled directions. They are separated by $\pi/4$, so one lies within $\pi/8$ of the gradient direction. Hence

$$\max_{\boldsymbol{u} \in \mathcal{U}_8} |\boldsymbol{g} \cdot \boldsymbol{u}| \geq |\boldsymbol{g}| \cos(\pi/8). \tag{A1}$$

~~which places the octagonal admissible set inside the circular slope limit. The diagonal bound then becomes $\sqrt{2}\Delta h^{(0)}_{\max}$. This correction removes the directional bias from the target slope constraint.~~ If all sampled ratios are bounded by $\tan\theta\cos(\pi/8)$, then $|\boldsymbol{g}| \leq \tan\theta$. The corresponding elevation-difference bounds are $\Delta x \tan\theta \cos(\pi/8)$ for cardinal pairs and $\sqrt{2}$ times this value for diagonal pairs. The common scaling tightens both sets of bounds conservatively for any orientation of a plane; it does not remove the stencil's directional anisotropy. The angle of the initial pairwise bounds is θ_{eff} in Eq. (3).

A2 Pseudocode

The pseudocode below summarises the algorithm with the parameter values used for the terrain members analysed in this paper.

Algorithm A1 SCO v1.0

Input: $h(n_x, n_y)$ terrain elevation (m); landmask(n_x, n_y); Δx grid spacing (m); θ target slope angle (°); ~~r, t~~ $r = 3, t = 5$ frozen-rim and transition widths; $\beta = 0.97$, $f_{\min} = 0.30$, max_outer $= 10$, max_sweeps $= 500$, inner_tol $= 0.1$ m, outer_tol_deg $= 0.01°$
Output: $h(n_x, n_y)$ adjusted terrain elevation; nominal-target acceptance flag

1. Compute base cardinal bound: $\Delta h^{(0)}_{\max} \leftarrow \Delta x \cdot \tan(\theta) \cdot \cos(\pi/8)$
2. Build mobility-weight field $w(n_x, n_y)$:
   $w = 0$ where landmask < 0.5 [water]
   $w = 0$ in outermost r rows and columns [frozen rim]
   $w =$ cosine taper across next t rows and columns [transition zone]
   $w = 1$ elsewhere [interior land]
3. Initialise tightening factors: $f(i,j) \leftarrow 1$ for all (i,j)
4. Define active interior mask: interior $\leftarrow (w > 0.5)$; set acceptance flag to false
5. **for** round $= 1$ to max_outer **do**
   5a. Update local bounds: $\Delta h_{\max}(i,j) \leftarrow f(i,j) \cdot \Delta h^{(0)}_{\max}$
   Initialise $E_{\text{prev}} \leftarrow \infty$, $c \leftarrow 0$
   5b. **for** sweep ~~$= 1$~~ $s = 1$ to max_sweeps **do**
   Set $E_s \leftarrow 0$
   for each pair class (horiz., vert., main diag., anti-diag.) **do**
   for each ~~non-overlapping pair~~ red–black subset of pairs (p, q) **do** (vectorised)
   $L_{pq} \leftarrow \min(\Delta h_{\max}(p), \Delta h_{\max}(q))$ [$\times\sqrt{2}$ for diag.]
   $\delta \leftarrow h(q) - h(p)$
   if $|\delta| > L_{pq}$ and $w(p) + w(q) > 10^{-6}$ **then**
   $e \leftarrow \delta - \text{sgn}(\delta) \cdot L_{pq}$
   $E_s \leftarrow \max(E_s, \max|e|)$
   $h(p) \leftarrow h(p) + e \cdot w(p)/(w(p) + w(q))$
   $h(q) \leftarrow h(q) - e \cdot w(q)/(w(p) + w(q))$
   ~~Diagnose max pairwise exceedance over active pairs~~ **if** $E_s \geq 0.999 E_{\text{prev}}$ **then** $c \leftarrow c + 1$; **else** $c \leftarrow 0$
   Set $E_{\text{prev}} \leftarrow E_s$
   if ~~max_exceedance $<$ inner_tol~~ $E_s <$ inner_tol or $c \geq 3$ **then** exit sweep loop
   5c. Diagnose $S(i,j)$ and $S_{\max,\text{int}}$ from updated h over interior points
   5d. **if** $S_{\max,\text{int}} \leq \theta +$ outer_tol_deg **then** set acceptance flag to true and exit outer loop
   5e. **for each** interior point where $S(i,j) > \theta$ **do**
   $f(i,j) \leftarrow \max[f(i,j) \cdot \beta \cdot \theta / S(i,j),\ f_{\min}]$
6. **return** h and acceptance flag

~~Boundary residuals are diagnosed separately and do not enter the outer tightening step. The octagonal correction, the mobility-weight field, the pairwise weighted projection, and the outer tightening together define the algorithm used here~~ Within each red–black subset, pairwise differences are evaluated before the endpoint contributions are accumulated. Pairs adjoining

frozen points enter the inner monitor when at least one endpoint is movable; points outside the active interior do not enter the outer acceptance test or local tightening.

Code and data availability. The SCO v1.0 source code is archived on Zenodo at https://doi.org/10.5281/zenodo.19501184 (Ma, 2026) under the GNU General Public License v3.0 or later. The archive includes the reference solver (`sco_terrain.py`), the unit-test suite (`test_sco_terrain.py`), the WRF namelist (`namelist.input`), and a worked example comprising a Fig. 1 generation script (`fig1_idealized.py`), a sample `geo_em.d02.nc` file, and a driver script (`run_example.py`) that demonstrates the full offline preprocessing workflow.

The simulations were performed with the Weather Research and Forecasting Model version 4.6.1 (Skamarock et al., 2019); the exact WRF-ARW v4.6.1 source code and the WPS used for terrain preprocessing are archived on Zenodo at https://doi.org/10.5281/zenodo.20809210 (WRF Community and NCAR, 2026). ERA5 reanalysis data used for initial and boundary conditions are available from the Copernicus Climate Data Store under the Creative Commons Attribution licence: hourly data on pressure levels at https://doi.org/10.24381/cds.bd0915c6 (Hersbach et al., 2023a) and on single levels at https://doi.org/10.24381/cds.adbb2d47 (Hersbach et al., 2023b); the corresponding ERA5 domain subset is included in the reproducibility archive. The static terrain for the 1 km inner domain is the 30 m ASTER Global Digital Elevation Model version 3, distributed by the NASA Land Processes Distributed Active Archive Center (LP DAAC) and available at https://doi.org/10.5067/ASTER/ASTGTM.003 (NASA/METI/AIST/Japan Spacesystems and U.S./Japan ASTER Science Team, 2019); the corresponding ASTER tile subset is likewise included in the reproducibility archive.

Near-surface verification uses hourly 10 m wind speed and 2 m temperature from the China Meteorological Administration (CMA) hourly multi-element surface observation dataset (product SURF_CHN_MUL_HOR), provided by the CMA National Meteorological Information Center. These raw observations are not publicly available, but can be obtained from the CMA Meteorological Data Service Centre (https://data.cma.cn/en) on reasonable request, including for the purposes of peer review.

The reproducibility archive on Zenodo at https://doi.org/10.5281/zenodo.20809228 (Ma et al., 2026) bundles the ERA5 domain subset and ASTER tile subset noted above with everything else needed to reproduce the near-surface verification without the raw observations: the `geo_em` static-terrain fields for all members and both domains, the WPS and WRF namelists, the derived verification statistics (per-station, per-member time-averaged RMSE and bias for 10 m wind and 2 m temperature, anonymized so that no raw observation values, station coordinates, or station identifiers are included), and a reproduction script (`make_table3.py`) that regenerates the Table 3 values and the Sect. 4.3 paired *t*-tests.

Author contributions. Y. Ma designed the SCO algorithm, developed the Python implementation, carried out the offline diagnostics, and wrote the manuscript. X. Jiang configured the WRF simulations and performed the ~~HPC~~ integrations using high-performance computing (HPC) resources. L. Mu supervised the project and contributed to the experimental design. Z. Heng contributed to station-data processing and quality control. All authors reviewed and edited the manuscript.

Competing interests. The authors declare that they have no conflict of interest.

Acknowledgements. The authors thank the China Meteorological Administration for providing surface observation data.

Financial support. This work was supported by the Sichuan Science and Technology Program (grant no. 2025YFNH0006), the National Natural Science Foundation of China (grant no. 42375160), the National Key Research and Development Program of China (grant no. 2023YFC3007501), the Guangdong Basic and Applied Basic Research Foundation (grant no. 2022A1515110841), the Shenzhen Fundamental Research Program (grant no. JCYJ20220530164400001), the Sichuan Science and Technology Program (grant no. 2024YFFK0110), and the Southwest Sichuan (Ya'an) Rainstorm Laboratory (grant no. CXNBYSYSZD202401).

References

Cannon, F., Carvalho, L. M. V., Jones, C., Norris, J., Bookhagen, B., and Kiladis, G. N.: Effects of topographic smoothing on the simulation of winter precipitation in High Mountain Asia, J. Geophys. Res. Atmos., 122, 1456–1474, https://doi.org/10.1002/2016JD026038, 2017.

Díaz-Fernández, J., Calvo-Sancho, C., Bolgiani, P., Sastre, M., López-Reyes, M., Fernández-González, S., and Martín, M. L.: Effect of complex orography on numerical simulations of a downburst event in Spain, Atmos. Res., 314, 107821, https://doi.org/10.1016/j.atmosres.2024.107821, 2025.

Hersbach, H., Bell, B., Berrisford, P., Hirahara, S., Horányi, A., Muñoz-Sabater, J., Nicolas, J., Peubey, C., Radu, R., Schepers, D., Simmons, A., Soci, C., Abdalla, S., Abellan, X., Balsamo, G., Bechtold, P., Biavati, G., Bidlot, J., Bonavita, M., De Chiara, G., Dahlgren, P., Dee, D., Diamantakis, M., Dragani, R., Flemming, J., Forbes, R., Fuentes, M., Geer, A., Haimberger, L., Healy, S., Hogan, R. J., Hólm, E., Janisková, M., Keeley, S., Laloyaux, P., Lopez, P., Lupu, C., Radnoti, G., de Rosnay, P., Rozum, I., Vamborg, F., Villaume, S., and Thépaut, J.-N.: The ERA5 global reanalysis, Q. J. Roy. Meteor. Soc., 146, 1999–2049, https://doi.org/10.1002/qj.3803, 2020.

Hersbach, H., Bell, B., Berrisford, P., Biavati, G., Horányi, A., Muñoz Sabater, J., Nicolas, J., Peubey, C., Radu, R., Rozum, I., Schepers, D., Simmons, A., Soci, C., Dee, D., and Thépaut, J.-N.: ERA5 hourly data on pressure levels from 1940 to present, Copernicus Climate Change Service (C3S) Climate Data Store (CDS) [data set], https://doi.org/10.24381/cds.bd0915c6, 2023a.

Hersbach, H., Bell, B., Berrisford, P., Biavati, G., Horányi, A., Muñoz Sabater, J., Nicolas, J., Peubey, C., Radu, R., Rozum, I., Schepers, D., Simmons, A., Soci, C., Dee, D., and Thépaut, J.-N.: ERA5 hourly data on single levels from 1940 to present, Copernicus Climate Change Service (C3S) Climate Data Store (CDS) [data set], https://doi.org/10.24381/cds.adbb2d47, 2023b.

Hong, S. Y., Noh, Y., and Dudhia, J.: A new vertical diffusion package with an explicit treatment of entrainment processes, Mon. Weather Rev., 134, 2318–2341, https://doi.org/10.1175/mwr3199.1, 2006.

Iacono, M. J., Delamere, J. S., Mlawer, E. J., Shephard, M. W., Clough, S. A., and Collins, W. D.: Radiative forcing by long-lived greenhouse gases: Calculations with the AER radiative transfer models, J. Geophys. Res., 113, D13103, https://doi.org/10.1029/2008JD009944, 2008.

Klemp, J. B., Skamarock, W. C., and Fuhrer, O.: Numerical consistency of metric terms in terrain-following coordinates, Mon. Weather Rev., 131, 1229–1239, https://doi.org/10.1175/1520-0493(2003)131<1229:NCOMTI>2.0.CO;2, 2003.

Le Bouëdec, E., Chemel, C., and Staquet, C.: Dealing with steep slopes when modeling stable boundary-layer flow in Alpine terrain, Q. J. Roy. Meteor. Soc., 151, e4835, https://doi.org/10.1002/qj.4835, 2025.

Ma, Y.: SCO v1.0: Slope-Constrained Orography for WRF terrain preprocessing (v1.0), Zenodo [code], https://doi.org/10.5281/zenodo.19501184, 2026.

Ma, Y., Jiang, X., Mu, L., and Heng, Z.: Reproducibility archive for "Slope-Constrained Orography (SCO v1.0) for explicit discrete-slope control in terrain preprocessing", Zenodo [data set], https://doi.org/10.5281/zenodo.20809228, 2026.

Ma, Y. and Liu, H.: Large-eddy simulations of atmospheric flows over complex terrain using the immersed-boundary method in the Weather Research and Forecasting Model, Bound.-Lay. Meteorol., 165, 421–445, https://doi.org/10.1007/s10546-017-0283-9, 2017.

Mahrer, Y.: An improved numerical approximation of the horizontal gradients in a terrain-following coordinate system, Mon. Weather Rev., 112, 918–922, https://doi.org/10.1175/1520-0493(1984)112<0918:AINAOT>2.0.CO;2, 1984.

NASA/METI/AIST/Japan Spacesystems and U.S./Japan ASTER Science Team: ASTER Global Digital Elevation Model V003, NASA EOSDIS Land Processes DAAC [data set], https://doi.org/10.5067/ASTER/ASTGTM.003, 2019.

Niu, G.-Y., Yang, Z.-L., Mitchell, K. E., Chen, F., Ek, M. B., Barlage, M., Kumar, A., Manning, K., Niyogi, D., Rosero, E., Tewari, M., and Xia, Y.: The community Noah land surface model with multiparameterization options (Noah-MP): 1. Model description and evaluation with local-scale measurements, J. Geophys. Res., 116, D12109, https://doi.org/10.1029/2010JD015139, 2011.

Park, S. H., Klemp, J. B., and Kim, J. H.: Hybrid mass coordinate in WRF-ARW and its impact on upper-level turbulence forecasting, Mon. Weather Rev., 147, 971–985, https://doi.org/10.1175/MWR-D-18-0334.1, 2019.

Raderschall, N., Lehning, M., and Schär, C.: Fine-scale modeling of the boundary layer wind field over steep topography, Water Resour. Res., 44, W09425, https://doi.org/10.1029/2007WR006544, 2008.

Raluy-López, E., Muñoz-Esparza, D., and Montávez, J. P.: A ~~Local Terrain Smoothing Approach for Stabilizing Microscale and High-Resolution Mesoscale Simulations: a Case Study Using~~ local terrain smoothing approach for stabilizing microscale and high-resolution mesoscale simulations: a case study using FastEddy® (v3.0) and WRF (v4.6.0), ~~EGUsphere [preprint], https://doi.org/10.5194/egusphere-2025-3744, 2025.~~ Geosci. Model Dev., 19, 5139–5154, https://doi.org/10.5194/gmd-19-5139-2026, 2026.

Sheridan, P., Xu, A., Li, J., and Furtado, K.: Use of targeted orographic smoothing in very high resolution simulations of a downslope windstorm and rotor in a sub-tropical highland location, Adv. Atmos. Sci., 40, 2043–2062, https://doi.org/10.1007/s00376-023-2298-0, 2023.

Skamarock, W. C., Klemp, J. B., Dudhia, J., Gill, D. O., Liu, Z., Berner, J., Wang, W., Powers, J. G., Duda, M. G., Barker, D. M., and Huang, X.-Y.: A description of the advanced research WRF version 4, NCAR Tech. Note NCAR/TN-556+STR, https://doi.org/10.5065/1dfh-6p97, 2019.

Tachikawa, T., Hato, M., Kaku, M., and Iwasaki, A.: Characteristics of ASTER GDEM version 2, in: 2011 IEEE International Geoscience and Remote Sensing Symposium, Vancouver, BC, Canada, 3657–3660, https://doi.org/10.1109/IGARSS.2011.6050017, 2011.

Thompson, G., Field, P. R., Rasmussen, R. M., and Hall, W. D.: Explicit forecasts of winter precipitation using an improved bulk microphysics scheme. Part II: Implementation of a new snow parameterization, Mon. Weather Rev., 136, 5095–5115, https://doi.org/10.1175/2008mwr2387.1, 2008.

WRF Community and NCAR: Weather Research and Forecasting (WRF) Model and WRF Preprocessing System (WPS) (WRF-ARW v4.6.1), Zenodo [code], https://doi.org/10.5281/zenodo.20809210, 2026.

Zängl, G., Gantner, L., Hartjenstein, G., and Noppel, H.: Numerical errors above steep topography: A model intercomparison, Meteorol. Z., 13, 69–76, https://doi.org/10.1127/0941-2948/2004/0013-0069, 2004.